

Nonperturbative calculation of exchange coupling parameters

Tomonori Tanaka* and Yoshihiro Gohda†

Department of Materials Science and Engineering, Institute of Science Tokyo, Yokohama 226-8502, Japan

(Dated: October 16, 2024)

Exchange coupling parameters J_{ij} within the Heisenberg model and its extensions are crucial for understanding magnetic behavior at the atomic level. To calculate J_{ij} from first principles, perturbative methods based on the magnetic force theorem (MFT), commonly referred to as the Liechtenstein's method, has been widely employed. However, the quantitative accuracy of J_{ij} obtained through this perturbative technique remains questionable. In this paper, we nonperturbatively calculate J_{ij} for several systems of both fundamental and applied significance, including perovskite SrMnO₃, neodymium-magnet compounds, and elemental 3d transition metals, and compare these results with those obtained using the conventional MFT-based method. The nonperturbative approach consistently yields reliable results, whereas the MFT-based method exhibits issues in both quantitative and, at times, qualitative accuracy. As discussed later in this paper, these discrepancies arise from neglected contributions within the MFT-based methods. Our nonperturbative scheme is highly versatile and offers strong prospects as a new platform for analyzing and designing spintronics materials, where developing accurate magnetic models is essential.

I. INTRODUCTION

Understanding magnetic interactions at the atomic level has become increasingly important with recent advancements in spintronics technology [1]. Currently, density functional theory (DFT) is the standard method for electronic structure calculations, effectively meeting these quantitative needs. However, DFT is inherently valid for ground-state properties. Therefore, to simulate magnetic states at finite temperatures and spin dynamics phenomena such as skyrmions and magnons, which are essential for practical applications, more coarse-grained computational models are required. One such approach is the lattice-spin model [2].

The lattice-spin model is a framework that focuses exclusively on spin degrees of freedom, excluding charge degrees of freedom, with the Heisenberg model and its extensions serving as representative examples. The quantitative accuracy of such models is governed by the model parameters, including exchange coupling parameters J_{ij} . Today, the evaluation of J_{ij} in the Heisenberg model from first principles has become common practice [3, 4]. The most popular method for determining J_{ij} is Liechtenstein's method, which is based on the perturbation theory [5, 6] referred to as the magnetic force theorem (MFT). The conventional MFT-based method and its family [3, 4, 7–10] have been applied to a wide range of magnetic materials and have provided microscopic understanding of interatomic magnetic interactions. However, recent theoretical studies have highlighted discrepancies between J_{ij} values obtained from MFT-based methods and those derived from nonperturbative (self-consistent) calculations in some materials, even for relatively small rotation angles of magnetic moments [11, 12]. Particularly noteworthy is the case of SrMnO₃ with the type-G antiferromagnetic state, where the signs of the J_{ij} at the first nearest neighbor obtained from the MFT-based method and the nonperturbative method were found to be contradictory [12]. Such an example raises a question about the

straightforward applicability of the MFT.

The fundamental principle of the MFT within DFT is based on the energy variation δE due to the infinitesimal rotations of magnetic moments as [13]

$$\begin{aligned}\delta E &= \delta^* E_{\text{band}} + \mathcal{O}(\delta n^2, \delta m^2) \\ &\approx \delta^* E_{\text{band}},\end{aligned}\quad (1)$$

where δn and δm represent the change in electron density and the longitudinal change in magnetization density, respectively. Here, $\delta^* E_{\text{band}}$ refers to the variation in band energy under conditions of fixed electron density and fixed magnetization magnitude, where only the direction of the magnetization is rotated. According to Eq. (1), MFT-based methods only consider the change in $\delta^* E_{\text{band}}$. The term $\mathcal{O}(\delta n^2, \delta m^2)$, consisting of the second order variations of the band energy and the double counting terms, can be neglected for infinitesimal rotations. Although this approximation widely used for evaluating J_{ij} , its validity must be reexamined for a more accurate description of finite-temperature magnetism, as the magnetic states of interest typically involve finite rotation angles.

In this study, we demonstrate the importance of nonperturbative evaluation of J_{ij} by applying it to several systems. The selected systems include perovskite SrMnO₃ and neodymium-magnet compounds, where conventional MFT-based methods have failed to produce accurate results, as well as elemental 3d transition metals. As pointed out in Ref. [12], a conventional MFT-based method cannot reproduce the energy variation due to the small rotation of magnetic moments in perovskite SrMnO₃ with the type-G antiferromagnetic state. In contrast, J_{ij} obtained through the nonperturbative method does not exhibit this inconsistency. We reveal that the failure of the conventional MFT-based method is due to significant changes in orbital occupancies, which are difficult to address using perturbative approaches (Sec. IV A). We also calculate the Curie temperatures of Nd₂Fe₁₄B and Nd₂Co₁₄B as representative permanent magnet compounds. It has been reported that an MFT-based method failed to reproduce the experimental results showing an increase in the Curie temperature with Co substitution in these permanent magnet compounds [14]. We demonstrate how the nonperturbative method consistently

* tanaka.t.bj@m.titech.ac.jp

† gohda.y.ab@m.titech.ac.jp

produces results that align with the experimental findings without contradictions (Sec. IV B). Finally, we systematically calculate J_{ij} for elemental $3d$ transition metals with bcc and fcc structures, and compare these results with those obtained by an MFT-based method. We find the contribution of $\mathcal{O}(\delta n^2, \delta m^2)$ is not negligible for quantitative evaluations of J_{ij} , even with relatively small rotation angles of magnetic moments (Sec. IV C).

II. METHODS

A. Nonperturbative calculation of J_{ij} with supercells

The validity of an effective spin model depends on the system's symmetry and required energy accuracy. We use a classical spin model consisting of the lowest-order pairwise interactions throughout this study as

$$E(\{\hat{e}\}) = E_0 - \sum_{i \neq j} J_{ij} \hat{e}_i \cdot \hat{e}_j, \quad (2)$$

where E_0 is the reference energy, J_{ij} is the isotropic exchange coupling parameter between site i and j , and \hat{e}_i is a unit vector representing the orientation of the local magnetic moment on site i . This simplified model is valid when the influence of the system's anisotropy on the physical quantities of interest is small. The model parameters J_{ij} and E_0 can be determined by minimizing the residual sum of squares [15] defined as

$$\Delta E^2 = \frac{1}{N_{\text{data}}} \sum_{n=1}^{N_{\text{tot}}} \left(E_{\text{DFT}}^{(n)} - E_{\text{model}}^{(n)} \right)^2, \quad (3)$$

where $E_{\text{DFT}}^{(n)}$ is the energy obtained from DFT calculations for n -th magnetic configuration, $E_{\text{model}}^{(n)}$ is the energy related to the spin model, and N_{data} is the total number of magnetic configurations. In this study, we used the supercell method to model magnetic configurations. Thus, we hereinafter refer to this procedure as the (SC)² method (Self-Consistent SuperCell method) for convenience. In the practical calculations, we used the symmetry of the target systems to identify independent J_{ij} by using Spglib library [16].

The model parameters in Eq. (2) depend on how the magnetic configuration dataset is sampled. Our focus is on J_{ij} near stable or metastable magnetic configurations to compare them with those obtained from MFT-based methods. Therefore, we slightly tilted the direction of the magnetic moment on each atom from a (meta)stable magnetic configuration. Specifically, we used uniformly distributed random numbers on a spherical cap in the range of $0^\circ \leq \theta \leq \theta_{\text{max}}$, while azimuthal angles were unrestricted. Magnetic configurations were sampled until the parameters converged; typically, three times the number of independent J_{ij} magnetic configurations were used. It is straightforward to extend the above procedure if one wishes to sample more realistic magnetic configurations. For example, in Ref. [17], the magnetic configurations at finite temperatures are sampled using a combination of Monte Carlo simulations.

We note that the parameters J_{ij} in the (SC)² method involve a size effect similar to that in the direct method for phonon calculations; the parameters are not values between individual sites but between the periodic images of sites i and j . This size effect decreases as the supercell size increases. Therefore, we carefully check the convergence of J_{ij} with respect to the supercell size. Additionally, we distinguish the (SC)² method from approaches that rely on energy differences between completely different magnetic states, such as ferromagnetic and antiferromagnetic states. The latter method assumes that the magnetic coupling parameters remain constant regardless of the magnetic configuration. However, this assumption is questionable, particularly in many metallic systems where the magnitude of the magnetic moment can easily change. In contrast, J_{ij} calculated using the (SC)² method can account for the dependence of J_{ij} on the reference magnetic states.

B. Comparison with the spin-spiral method

We briefly review the differences between the (SC)² method and the spin-spiral method, both of which are nonperturbative approaches. The spin-spiral method, based on the generalized Bloch's theorem [18], is another procedure for sampling magnetic configurations [11]. Subsequently, exchange coupling parameters J_{ij} are evaluated to reproduce the energies of sampled spin-spiral states. A major advantage of this method is that it requires only a minimal magnetic unit cell, thus keeping computational costs relatively low. There are, however, some shortcomings that do not exist in the (SC)² method. For example, the spin-spiral method ignores the disorder caused by the excitation of multiple spin wave modes and the impact of this disorder on the electronic state, which is inevitable at finite temperatures. Moreover, spin-orbit coupling cannot be used in conjunction with the spin-spiral method because it breaks the translational symmetries assumed in the generalized Bloch's theorem.

We also note the extendability of the (SC)² method. First, the (SC)² method is not limited to evaluating the isotropic lowest-order interaction J_{ij} . For instance, Antal and co-workers have evaluated tensor-formed exchange coupling parameters, fourth-order interaction parameters, and on-site anisotropy parameters for a Cr trimer on Au(111) surface while considering spin-orbit coupling [15]. Second, the effect of lattice vibrations on exchange coupling parameters can also be calculated straightforwardly, as demonstrated in Ref. [17]. Notably, the direct modeling of atomic displacements due to lattice vibrations in a supercell is a feature not available in the spin-spiral method with a minimal cell. The current limitation of the (SC)² method compared to conventional methods is its higher computational cost and the difficulty in systematically improving magnetic models. However, we expect these problems can be overcome in future by combining the spin-cluster expansion [19] with the torque method which is utilizing a constraining magnetic field [11].

C. Relation between spin-cluster expansion

All the classical spin models, including the Heisenberg model used in this study, can be considered as a special case of the spin-cluster expansion method [19]. When the system's energy can be expressed in terms of a given set of atomic magnetic moment orientations $\{\hat{e}_i\}$, the spin-cluster expansion method offers a framework for describing the energy as

$$E(\{\hat{e}_i\}) = E_0 + \sum_{\alpha} \sum_l \sum_m J_{\alpha lm} \Phi_{\alpha lm}(\{\hat{e}_i\}), \quad (4)$$

where $J_{\alpha lm}$ is the cluster interaction coefficient and $\Phi_{\alpha lm}$ represents the cluster function regarding cluster set α defined as

$$\Phi_{\alpha lm}(\{\hat{e}_i\}) = \sum_{i \in \alpha} y_{l_1 m_1}(\hat{e}_1) \dots y_{l_M m_M}(\hat{e}_M), \quad (5)$$

where y_{lm} is the spherical harmonics with indices (l, m) . Note that y_{lm} is defined in terms of the conventional spherical harmonics Y_{lm} as

$$y_{lm} = \sqrt{4\pi} Y_{lm}. \quad (6)$$

The inner product between two spins ($\hat{e}_i \cdot \hat{e}_j$) in the Heisenberg model incorporated into the spin-cluster expansion as follows:

$$\hat{e}_i \cdot \hat{e}_j = \frac{1}{3} \sum_{m=-1}^1 y_{1m}^*(\hat{e}_i) y_{1m}(\hat{e}_j). \quad (7)$$

This relationship is straightforwardly derived from the spherical harmonics addition theorem;

$$P_l(\hat{e}_i \cdot \hat{e}_j) = \frac{1}{2l+1} \sum_{m=-l}^l y_{lm}^*(\hat{e}_i) y_{lm}(\hat{e}_j), \quad (8)$$

where P_l denotes the l -th Legendre polynomial. Although the cluster interaction coefficients $\{J_{\alpha lm}\}$ are independent of the sampling spin orientation space in the limit of infinite clusters, in practice, we have to truncate with finite number of terms. As a result, the cluster expansion coefficients exhibit a dependence on both the sampling spin orientation space and the choice of clusters. This can be understood by noting that J_{ij} in the Heisenberg model depends on the reference magnetic state. When J_{ij} parameters have a dependence on sampling spin orientation spaces, this arises from contributions beyond the terms included in the Heisenberg model. In other words, the dependence of J_{ij} on the sampling spin orientation space results from the renormalization of higher-order contributions to accurately reproduce the energy within that space. This discussion is revisited in Sec. IV C, with respect to the impact of self-consistency.

III. COMPUTATIONAL CONDITIONS

A. DFT calculations in the (SC)² method

In the (SC)² method, we employed constrained noncollinear spin DFT within the projector augmented-wave method [20] as

implemented in the VASP package [21, 22]. The constrained local moment approach was employed to fix the direction of the atomic magnetic moments, while the magnitudes of the magnetic moments were allowed to relax. As the exchange-correlation functional, we used two generalized gradient approximations: PBEsol [23] for SrMnO₃, and PBE [24] for neodymium-magnet compounds and elemental 3d transition metals. These choices were made to facilitate comparisons with previous studies [12, 14]. The energy convergence criterion was set to 10⁻⁷ eV/atom. The spin-orbit coupling was not incorporated throughout this study. Other system-dependent conditions are described separately below.

1. SrMnO₃ with the type-G antiferromagnetic state

The plane-wave cutoff was set to 680 eV, and a k -grid spacing of approximately 0.17 Å⁻¹ in each reciprocal vector was used. To incorporate on-site Coulomb interactions, we applied the DFT+ U method [25] using $U_{\text{eff}} = 3.0$ eV [12]. We used two lattice constants following Ref. [12], specifically $a/a_{\text{eq}} = 1.0$ and 1.05, where the equilibrium lattice constant $a_{\text{eq}} = 3.79$ Å was adopted. A $2 \times 2 \times 2$ cubic cell (containing 40 atoms) was used. The radii of the atomic spheres, to which the constrained magnetic field was applied (VASP parameter RWIGS), were set to 2.0 Å for Sr, 1.2 Å for Mn, 0.7 Å for O.

2. Nd₂Fe₁₄B and Nd₂Co₁₄B

The plane-wave cutoff was set to 350 eV, and a k -grid spacing of approximately 0.18 Å⁻¹ in each reciprocal vector was used. Lattice constants were set to experimental values [26, 27], whereas internal atomic coordinates are optimized. The radii of the atomic spheres for the constrained magnetic field were set as 1.5 Å for Nd, 1.2 Å for Fe and Co, 0.8 Å for B. We used $1 \times 1 \times 1$ unit cell (containing 68 atoms). Although this relatively small unit cell introduces large size effect in the evaluation of J_{ij} itself, it does not pose major issues for the evaluation of the Curie temperature using the mean-field approximation [28] employed later. The size effect causes interactions with distant equivalent atomic pairs to be incorporated into the J_{ij} of nearby pairs. However, since the mean-field approximation eventually sums all J_{ij} between equivalent pairs, the size effect does not pose a problem for the evaluation of the Curie temperature.

3. Elemental 3d transition metals with bcc and fcc structures

The plane-wave cutoff was set to 350 eV, and a k -grid spacing of approximately 0.18 Å⁻¹ in each reciprocal vector was used. We used $4 \times 4 \times 4$ cubic supercells for bcc and $3 \times 3 \times 3$ cubic supercells for fcc. The radii of the atomic spheres were set to half the nearest neighbor distance in each system. The dependence of J_{ij} on the radii of the atomic spheres and the convergence with respect to the supercell size were summarized in

TABLE I. Lattice constants (a), reference magnetic configurations, and the magnitude of magnetic moment $|m|$ per atomic site of elemental $3d$ transition metals. The notations AFM and FM denote antiferromagnetic and ferromagnetic, respectively. Lattice constants are obtained by structure optimization, except for fcc Mn (see the main text).

System	a (Å)	Reference magnetic configuration	$ m $ (μ_B)
bcc			
Cr	2.85	Type-I AFM	1.04
Mn	2.79	FM	0.89
Fe	2.83	FM	2.21
Co	2.80	FM	1.81
Ni	2.80	FM	0.59
fcc			
Mn	3.86	FM	2.98
Fe	3.64	FM	2.60
Co	3.51	FM	1.65
Ni	3.52	FM	0.62

the Supplementary Information. The lattice constants, reference magnetic configurations, and magnetic moments within an atomic site are provided in Table. I. Note the following two points: For bcc Cr, the reference magnetic state was assumed to be the type-I antiferromagnetic state in our calculations, although a spin-density wave is observed in experiments; for fcc Mn, we adopted a relatively large lattice constant (3.86 Å) to be a ferromagnetic state, because this system exhibits a nonmagnetic state in a wide range of volumes around the equilibrium point.

B. MFT-based method

The family of MFT-based methods has been implemented using various basis sets and DFT packages. To minimize the dependence on basis sets, we adopted tight-binding models with Wannier functions constructed from the same VASP package [21, 22] in the case of the (SC)² method. The Wannier functions were generated using the Wannier90 package [29], and the TB2J package [9] was subsequently employed to evaluate J_{ij} . For the results concerning elemental $3d$ transition metals, we also present J_{ij} values obtained with different three upper bounds of integration with respect to band energy: $\varepsilon_F - 0.1$ eV, ε_F , and $\varepsilon_F + 0.1$ eV (Please see Ref. [6, 9] for details and definitions). This approach was taken to determine whether the differences between the conventional MFT-based method and the (SC)² method are attributable to sensitivity to the integration limits.

Unfortunately, in the case of neodymium-magnet compounds, the evaluations of J_{ij} via constructing Wannier functions are very computationally demanding. Thus we alternatively employed the KKR-Green function method implemented in AkaiKKR package [30] as described in Ref. [14]. The same structural parameters used in the (SC)² method were applied in all cases.

C. Classical Monte Carlo simulations

Classical Monte Carlo simulations, implemented in the EspinS package [31], were carried out to numerically evaluate the magnetic phase transition temperatures of elemental $3d$ transition metals. Interaction shells up to the 10th nearest neighbor for bcc structures and the 7th nearest neighbor for fcc structures were considered for J_{ij} . The results of the (SC)² method were calculated using J_{ij} in $4 \times 4 \times 4$ supercell for bcc and $3 \times 3 \times 3$ supercell for fcc. For both structures, $16 \times 16 \times 16$ sites were adopted, with 300,000 steps for equilibration and 2,000,000 steps for sampling. The magnetic phase transition temperatures were defined as the temperature at which the specific heat exhibits a peak.

IV. RESULTS

A. SrMnO₃ with the type-G antiferromagnetic state

Perovskite SrMnO₃ exhibits multiferroicity [32] and has therefore attracted a lot of interest for new information technologies. In addition, the strong dependence of J_{ij} between Mn atoms on strain, which induces magnetic phase transitions, was experimentally examined [33]. Thus the quantitative evaluation of J_{ij} is crucial for reliable materials and device design with sensitive magnetic properties. A recent study, however, demonstrated that the J_{ij} of SrMnO₃ obtained from the MFT is qualitatively different from the results of self-consistent calculations [12]; under isotropic volume expansion, the MFT-based method predicted a negative first-nearest exchange coupling parameter J_{01} in the type-G antiferromagnetic state, but it should be positive according to self-consistent calculations. Here, we reexamine their results and discuss the origin of the difference in J_{01} in terms of $\mathcal{O}(\delta n^2, \delta m^2)$ in Eq. (1).

Figure 1 shows J_{01} between Mn atoms in cubic SrMnO₃ for different lattice constants $a/a_{\text{eq}} = 1.0$ and 1.05 (the J_{ij} values for more distant atomic pairs are summarized in the Supplementary Information). In addition to the results from the MFT-based and the (SC)² methods, we also present results from a total energy method, where J_{01} is calculated from the energy difference between the type-G antiferromagnetic and ferromagnetic states as follows:

$$J_{01} = \frac{E_{\text{total}}^{\text{AFM}} - E_{\text{total}}^{\text{FM}}}{2N}, \quad (9)$$

where N is the number of equivalent Mn-Mn bonds at the first-nearest neighbor (the prefactor 2 in the numerator is due to the double counting in each bond as defined in Eq. (2)), $E_{\text{total}}^{\text{AFM}}$ and $E_{\text{total}}^{\text{FM}}$ are the total energies of the type-G antiferromagnetic and ferromagnetic states, respectively. This total energy method makes it easy to see the relative energy difference between the two magnetic states (note that J_{ij} at the second-nearest neighbor and beyond are sufficiently small relative to the one at the first-nearest neighbor). As reported in Ref. [12], the MFT gives negative J_{01} (favoring antiferromagnetic coupling) for both lattice constants. However, J_{01}

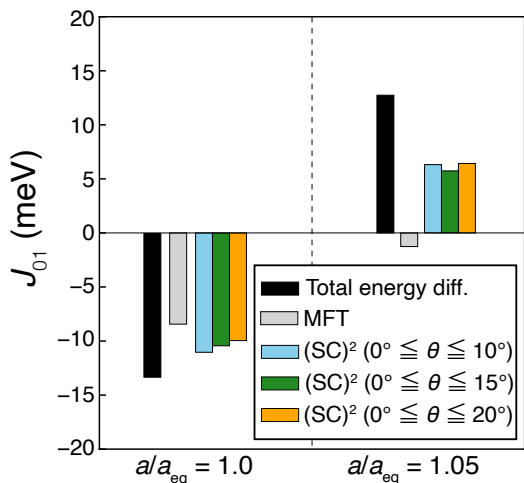


FIG. 1. Exchange coupling parameters at the first-nearest neighbor Mn-Mn pair J_{01} in cubic SrMnO₃ with the type-G antiferromagnetic state. The black and gray bars represent the results obtained from the total energy method in Eq. (9) and the MFT-based method, respectively. The other colored bars show the results from the (SC)² method with three difference upper bounds for the polar angle θ : 10° (blue), 15° (green), and 20° (orange). The lattice constants were set to $a/a_{\text{eq}} = 1.0$ and 1.05, where $a_{\text{eq}} = 3.79$ Å.

for $a/a_{\text{eq}} = 1.05$ should be positive as indicated by the total energy method. On the other hand, the (SC)² method correctly reproduced the change in the sign of J_{01} with volume expansion.

To examine the origin of the inconsistencies in the MFT-based method, we focus on the underlying electronic structure. Figures 2 (a) and (b) show the element-decomposed band dispersions of SrMnO₃ with and without the rotation of Mn magnetic moments ($\alpha = 10^\circ$ and 0°). For $a/a_{\text{eq}} = 1.0$, the band gap remains open, regardless of the magnetic moment rotation (Fig. 2 (a)). In contrast, for $a/a_{\text{eq}} = 1.05$, the band gap closes, and flat bands consisting of Mn and O states appear near the Fermi level along the $\Gamma - X$ line (upper panel of Fig. 2 (b)). Upon rotating magnetic moments, the degenerate Mn bands split into occupied and unoccupied states, while the occupied O bands near the Γ point shift into unoccupied state (lower panel of Fig. 2 (b)). Consequently, the changes in electron density associated with the rotation of Mn magnetic moments differ significantly before and after the volumetric expansion. Figure 3 shows the charge density differences $\Delta n(\mathbf{r})$ resulting from the rotation of Mn magnetic moments for $a/a_{\text{eq}} = 1.0$ and 1.05, defined as

$$\Delta n(\mathbf{r}) = n^{\alpha=10^\circ}(\mathbf{r}) - n^{\alpha=0^\circ}(\mathbf{r}), \quad (10)$$

where $n^{\alpha=\theta}(\mathbf{r})$ represents the electron density at position \mathbf{r} when magnetic moments are rotated by an angle θ . In the case of $a/a_{\text{eq}} = 1.05$ (Fig. 10(a)), we can see a large charge density difference at the Mn and O sites compared with the case of $a/a_0 = 1.0$ (Fig. 10(a)), due to the change in the orbital occupations described above. These behaviors of charge density difference are directly related to the magnitude of the contribution of $\mathcal{O}(\delta n^2, \delta m^2)$ in Eq. (1).

The failure of the MFT-based method likely arises from the inherent limitations of perturbation theory within Kohn-Sham theory. While perturbation theory provides the energy shift in each Kohn-Sham state due to perturbations, it assumes that the occupation numbers of all states remain unchanged. Consequently, in a system such as SrMnO₃ for $a/a_0 = 1.05$ even a rotation angle of 10° exceeds the applicability of the MFT. Therefore, in a system such as expanded SrMnO₃, even a rotation angle $\alpha = 10^\circ$ is far from the applicability of the MFT. According to Ref. [12], the practical applicable rotation angle for the MFT-based method appears to be significantly smaller than $\alpha = 10^\circ$ (which corresponds to 170° in the definition provided in Ref. [12]).

B. Nd₂Fe₁₄B and Nd₂Co₁₄B

Evaluation of J_{ij} plays an important role in the materials design of magnet compounds, because the stronger exchange couplings suppress demagnetization due to temperature, i.e., large J_{ij} values lead to higher Curie temperatures (T_C). Nevertheless, previous methods based on the MFT for evaluating T_C through J_{ij} of magnet compounds have been unsatisfactory in terms of quantitative evaluation; the MFT-based method failed to reproduce the increase in T_C when Co was substituted with Fe in Nd₂Fe₁₄B [14]. Magnetic interactions are important not only for understanding existing permanent magnets [36, 37] but also for exploring new magnetic compounds [38]. This problem, therefore, must be resolved for the reliable materials design of magnet compounds.

Figure 4 shows the differences between T_C values of Nd₂Fe₁₄B and Nd₂Co₁₄B. Note that the ferromagnetic ground state is assumed as a reference state in both the MFT-based method and the (SC)² method. As reported in Ref. [14], the MFT-based method cannot reproduce the increase in T_C when Fe is substituted with Co. Although this disagreement with experimental results can also be observed in the results from the (SC)² method for θ in the range of $0^\circ \leq \theta \leq 10^\circ$, a correct trend is obtained with increasing θ_{max} ; T_C of Nd₂Co₁₄B becomes larger than that of Nd₂Fe₁₄B when $\theta_{\text{max}} = 30^\circ$. This is because the decrease in T_C due to magnetic disordering is greater for Nd₂Fe₁₄B than for Nd₂Co₁₄B (absolute values of T_C are summarized in the Supplementary Information).

The above discussion emphasizes the limitation of MFT-based methods for the evaluation of T_C . Nevertheless, due to their convenience, MFT-based methods have been recognized as a standard tool for evaluating the composition dependence of T_C or T_C itself in magnet compounds. Our results clearly demonstrate that this convention does not hold, as the T_C strongly depends on the extent of magnetic disordering, at least for these systems. Of course, more quantitative evaluations, including other temperature effects, are needed to conclude the cause of the disagreement in T_C between theory and experiments. For example, Nd₂Fe₁₄B is reported to exhibit strong magnetism-dependent phonons [41], which are shifts of phonon frequencies due to magnetic disordering. As we previously pointed out in Ref. [42], the magnetism-dependent phonons affect the determination of equilibrium

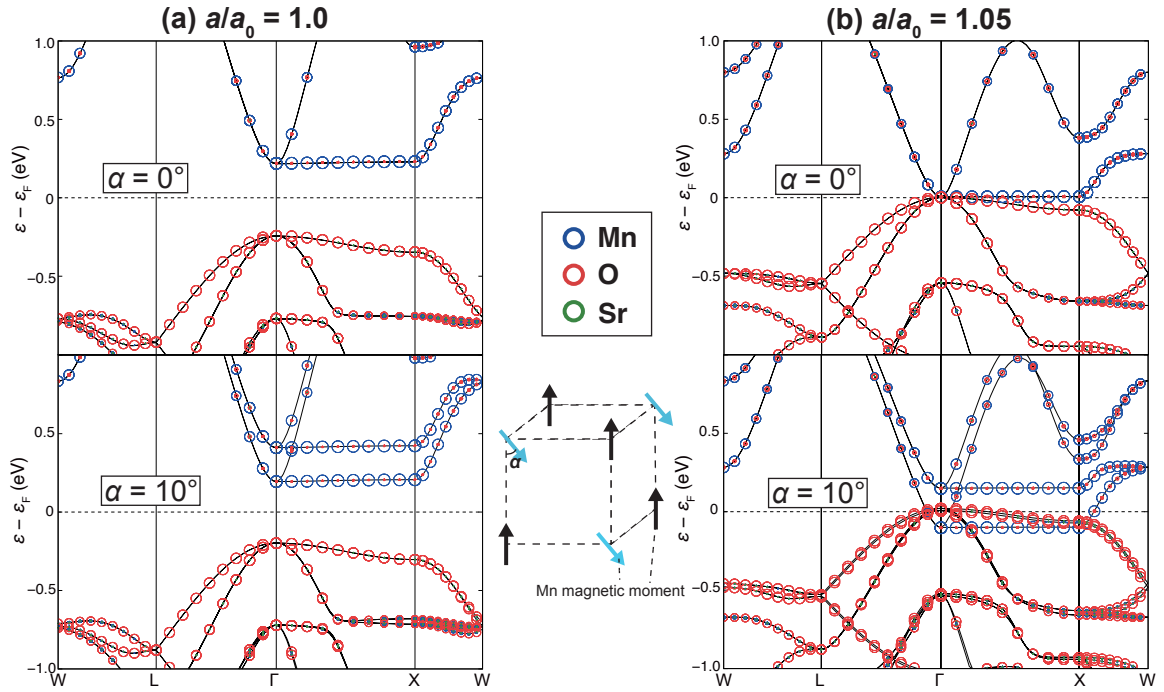


FIG. 2. Element-decomposed band dispersions of SrMnO_3 with and without rotation of Mn magnetic moments, as illustrated in the inset. Panel (a) corresponds to the equilibrium lattice constant $a/a_{\text{eq}} = 1.0$, whereas panel (b) corresponds to $a/a_{\text{eq}} = 1.05$. The blue, red, and green circles denote the contributions from Mn, O, and Sr, respectively. The band dispersions and the element contributions were plotted by using VASPKIT [34].

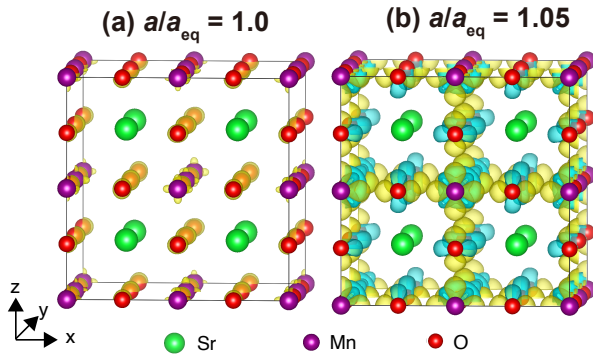


FIG. 3. Charge density differences $\Delta n(\mathbf{r})$ in SrMnO_3 as defined in Eq. (10) between rotation angles $\alpha = 10^\circ$ and $\alpha = 0^\circ$, drawn using VESTA software [35]. Panel (a) corresponds to the equilibrium lattice constant $a/a_{\text{eq}} = 1.0$, whereas panel (b) corresponds to $a/a_{\text{eq}} = 1.05$. The isosurface levels represented in yellow and blue are set to $+2 \times 10^{-5}$ and $-2 \times 10^{-5} \text{ bohr}^{-3}$, respectively.

magnetic states, and resulting in changes in the theoretical T_C . In addition, the direct impact of lattice vibrations on J_{ij} would affect T_C [17]. Although further investigation incorporating other temperature effects is necessary, our results clearly demonstrate that the straightforward application of the MFT cannot account for the concentration dependence of T_C in the $\text{Nd}_2(\text{Fe}, \text{Co})_{14}\text{B}$ system.

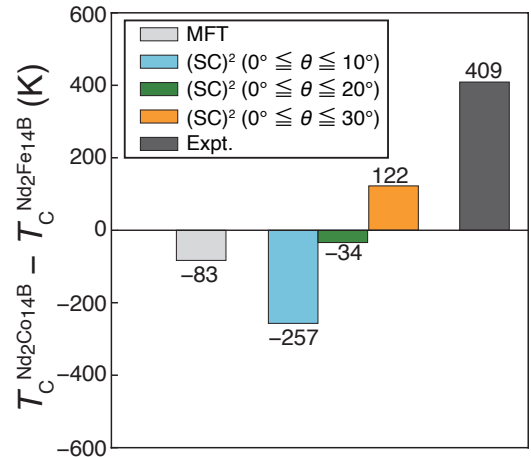


FIG. 4. Differences in the Curie temperatures T_C of $\text{Nd}_2\text{Co}_{14}\text{B}$ and $\text{Nd}_2\text{Fe}_{14}\text{B}$. The gray and black bars represent values obtained by the MFT-based method and experiments, respectively. The blue, green, and orange bars indicate values obtained by the $(\text{SC})^2$ method, with the upper bound of θ set to 10° , 20° , and 30° , respectively. Theoretical values are obtained by the mean-field approximation. Experimental values were taken from Ref. [39, 40].

C. Elemental 3d transition metals with bcc and fcc structures

Figures 5 (a)-(e) and 6 (a)-(d) show the J_{ij} of 3d transition metals for bcc and fcc structures, respectively. Generally,

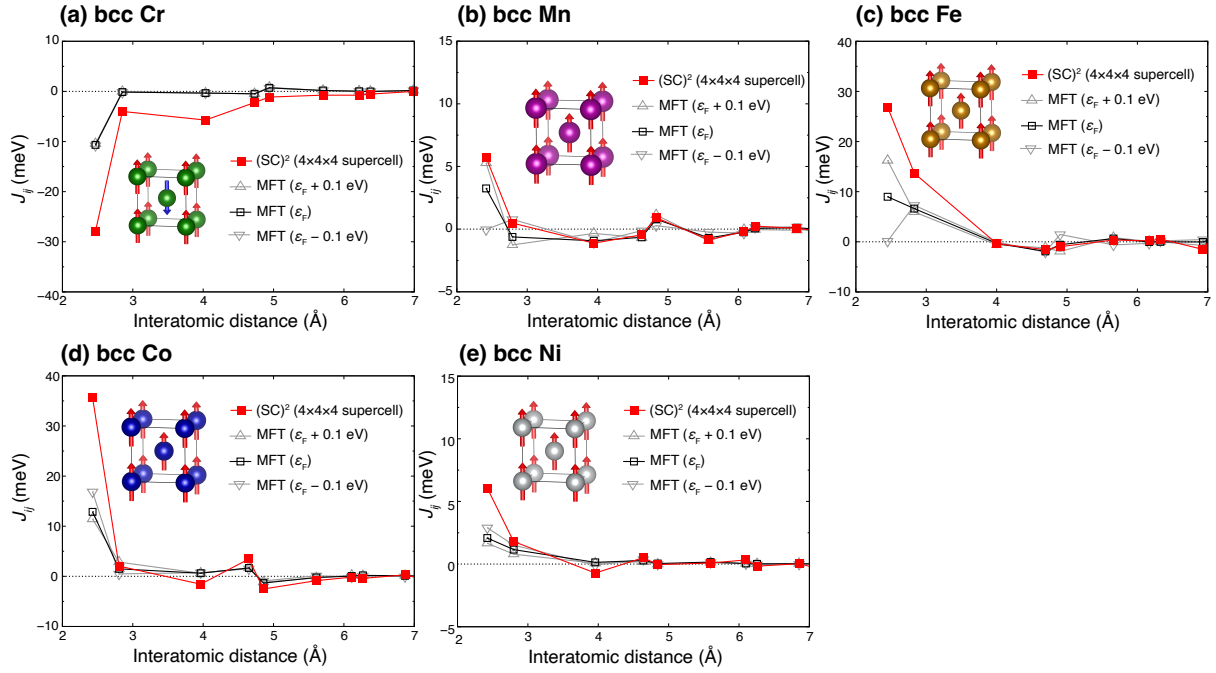


FIG. 5. Exchange coupling parameters J_{ij} in (a) bcc Cr, (b) bcc Mn, (c) bcc Fe, (d) bcc Co, and (e) bcc Ni. The results of the $(SC)^2$ method were obtained using a θ range of $0 \leq \theta \leq 10^\circ$. In the $(SC)^2$ method, a $4 \times 4 \times 4$ body-centered-cubic supercell containing 128 atoms was used. In the MFT-based method, we present results for three different upper bound of integration with respect to band energy: $\varepsilon_F - 0.1$ eV, ε_F , and $\varepsilon_F + 0.1$ eV. The reference magnetic state in each system is also shown using VESTA software [35].

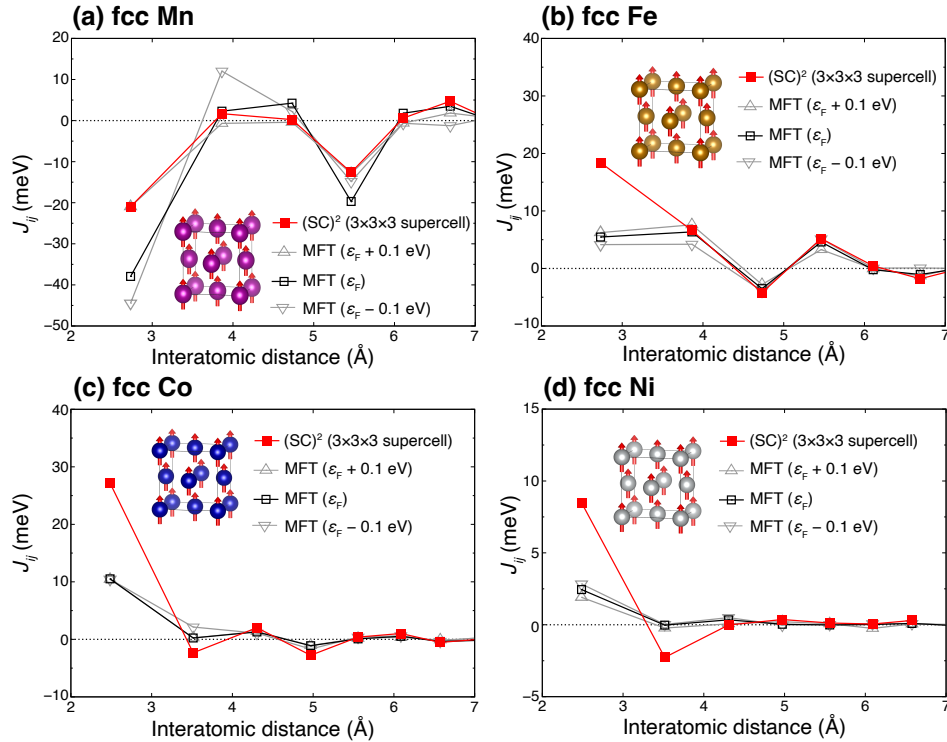


FIG. 6. Exchange coupling parameters J_{ij} in (a) fcc Mn, (b) fcc Fe, (c) fcc Co, and (d) fcc Ni. The results of the $(SC)^2$ method were obtained using a θ range of $0 \leq \theta \leq 10^\circ$. In the $(SC)^2$ method, a $3 \times 3 \times 3$ face-centered-cubic supercell containing 108 atoms was used. In the MFT-based method, we present results for three different upper bound of integration with respect to band energy: $\varepsilon_F - 0.1$ eV, ε_F , and $\varepsilon_F + 0.1$ eV. The reference magnetic state in each system is also shown using VESTA software [35].

J_{ij} values from the second nearest neighbor onwards show relatively good agreement between the two methods. However, significant differences in exchange coupling parameters at the first-nearest neighbors J_{01} are remarkable between the two methods in all of the systems. In particular, the differences in systems, except for bcc Mn and fcc Mn, cannot be explained the sensitivity to the integration limits with respect to band energy in the MFT-based method. We further investigate the origin of the large discrepancies in the following parts.

We calculated the change in J_{01} as the maximum rotation angle θ_{\max} was varied from 10° to 20° , as shown in Fig. 7. Systems with a large difference in J_{ij} between the nonperturbative method and the MFT-based method tend to also have a large angular dependence of J_{01} . As discussed in Sec. II C, the angular dependence of J_{01} (i.e., the dependence on the sampling spin orientation space) results from the renormalization of higher-order contributions beyond the Heisenberg model. Here, we demonstrate how the angular dependence of J_{ij} arises by using the biquadratic interaction $(-B_{ij}(\hat{e}_i \cdot \hat{e}_j)^2)$ as a representative of higher-order contributions. The spin hamiltonian is

$$\mathcal{H} = -J_{ij}\hat{e}_i \cdot \hat{e}_j - B_{ij}(\hat{e}_i \cdot \hat{e}_j)^2. \quad (11)$$

Energy as a function of θ_{\max} becomes

$$E = -J_{ij}\langle\hat{e}_i \cdot \hat{e}_j\rangle_{\theta_{\max}} - B_{ij}\langle(\hat{e}_i \cdot \hat{e}_j)^2\rangle_{\theta_{\max}}, \quad (12)$$

where $\langle\cdots\rangle_{\theta_{\max}}$ denotes an expectation value when the upper bound of θ is θ_{\max} . The angular dependent J_{ij} as $J_{ij}(\theta_{\max})$ arises when the biquadratic term is renormalized as

$$\begin{aligned} & -J_{ij}\langle\hat{e}_i \cdot \hat{e}_j\rangle_{\theta_{\max}} - B_{ij}\langle(\hat{e}_i \cdot \hat{e}_j)^2\rangle_{\theta_{\max}} \\ &= -\left(J_{ij} + B_{ij}\frac{\langle(\hat{e}_i \cdot \hat{e}_j)^2\rangle_{\theta_{\max}}}{\langle\hat{e}_i \cdot \hat{e}_j\rangle_{\theta_{\max}}}\right)\langle\hat{e}_i \cdot \hat{e}_j\rangle_{\theta_{\max}} \quad (13) \\ &= -J_{ij}(\theta_{\max})\langle\hat{e}_i \cdot \hat{e}_j\rangle_{\theta_{\max}}, \end{aligned}$$

where

$$J_{ij}(\theta_{\max}) = J_{ij} + B_{ij}\frac{\langle(\hat{e}_i \cdot \hat{e}_j)^2\rangle_{\theta_{\max}}}{\langle\hat{e}_i \cdot \hat{e}_j\rangle_{\theta_{\max}}}, \quad (14)$$

$$\begin{aligned} \frac{\langle(\hat{e}_i \cdot \hat{e}_j)^2\rangle_{\theta_{\max}}}{\langle\hat{e}_i \cdot \hat{e}_j\rangle_{\theta_{\max}}} &= \frac{2}{\sin^4\theta_{\max}} \\ &\times \left[\left(-\frac{3}{4}\cos\theta_{\max} + \frac{1}{12}\cos 3\theta_{\max} + \frac{2}{3}\right)^2 \right. \\ &\left. + \frac{2}{9}(1 - \cos^3\theta_{\max})^2 \right]. \quad (15) \end{aligned}$$

The derivation of $\langle(\hat{e}_i \cdot \hat{e}_j)^2\rangle_{\theta_{\max}}/\langle\hat{e}_i \cdot \hat{e}_j\rangle_{\theta_{\max}}$ is described in the Supplementary Information. The biquadratic interaction can also be evaluated within the MFT. However, we stress that the typical values of the $|B_{ij}|$ obtained from the MFT-based method (~ 5 meV for bcc Fe, ≤ 0.1 meV for hcp Co and fcc Ni [43]) cannot completely explain the large angular dependence of $J_{ij}(\theta_{\max})$; if the change in $|J_{ij}(\theta_{\max})|$ when θ_{\max} increases from 10° to 20° is 1 meV, $|B_{ij}|$ becomes 24 meV. It is also unlikely that other higher-order terms derived from perturbative

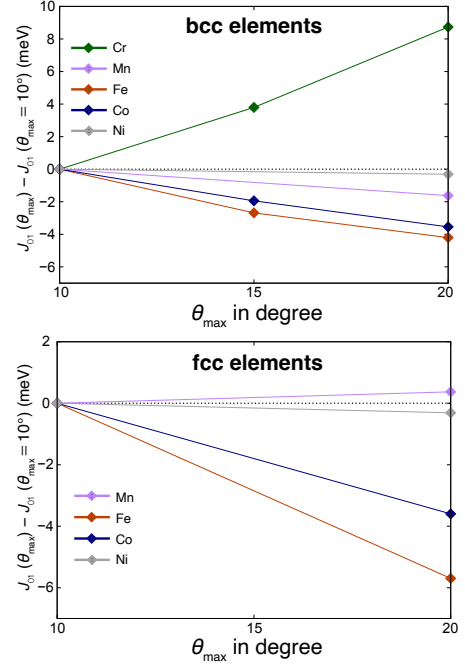


FIG. 7. Dependence of J_{01} of elemental $3d$ transition metals on the θ_{\max} . The origin of the vertical axis is the value of J_{01} when the range of θ is $0^\circ \leq \theta \leq 10^\circ$.

methods are the cause of the angular dependence [43]. This demonstrates two important points: (1) Even if MFT-based methods are formally extended and the precision of δ^*E_{band} is greatly improved, there is no guarantee that an accurate spin Hamiltonian can be derived. (2) To accurately construct an effective spin Hamiltonian, the effects of $\mathcal{O}(\delta n^2, \delta m^2)$ cannot be ignored, even for relatively small spin rotation angles.

We comment on the relatively large difference in J_{01} between the $(\text{SC})^2$ method and the MFT, despite the small angular dependence of J_{01} for bcc Ni (Fig. 5 (e)) and fcc Ni (Fig. 6 (d)). The cause of the difference might be the long-wavelength approximation in the MFT, which is less accurate for the evaluation of J_{ij} in strong itinerant magnetic materials as discussed in Ref. [44]; $J_{01} = 8.3$ meV in fcc Ni, obtained by going beyond the long-wavelength approximation [44], is consistent with the value obtained by the $(\text{SC})^2$ method (Fig. 6 (d)).

We also evaluated the magnetic phase transition temperatures by using classical Monte Carlo simulations, as shown in Fig. 8 with some experimental values. Reflecting the larger $|J_{01}|$, magnetic phase transition temperatures by the $(\text{SC})^2$ method are larger than those by the MFT except for fcc Mn. Although magnetic phase transition temperatures by the $(\text{SC})^2$ method seems to overestimate experimental values, the discrepancies will probably be lowered by considering further temperature effects, such as lattice vibrations [17] and the stabilization of paramagnetic states by magnetism-dependent phonons [42, 47], already described in Sec. IV B. Thus, the tendency to overestimate T_C when lattice vibration effects are neglected reflects a correct trend and further validates the non-

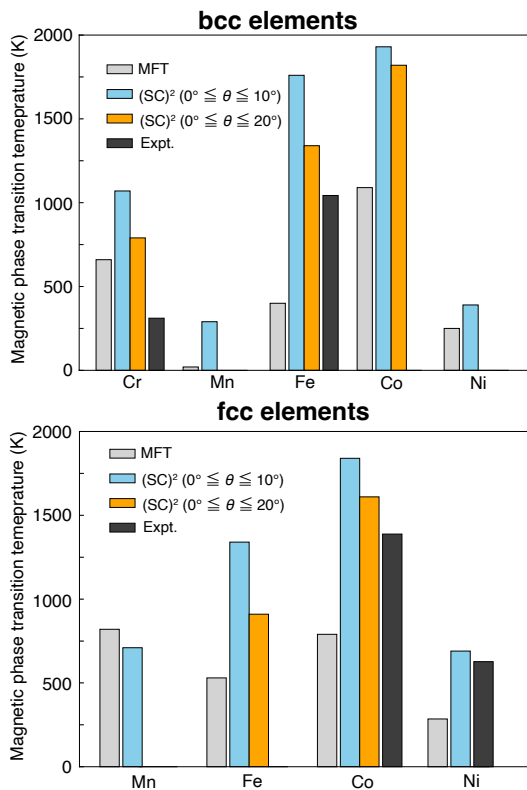


FIG. 8. Magnetic phase transition temperatures of elemental $3d$ metals obtained by the classical Monte Carlo simulations. For the systems that exhibit a large angular dependence of J_{01} in Fig. 7, the results for the angle range $0^\circ \leq \theta \leq 20^\circ$ are also shown. Experimental values are also arranged for comparison [45]. The results obtained using the MFT-based method are based on J_{ij} values calculated with the upper limit of the band energy set to ε_F . Note that the experimental value of bcc Cr is the one for the antiferromagnetic spin-density wave state [46] whereas calculated values here are those for the type-I antiferromagnetic state as illustrated in Fig. 5 (a).

perturbative method.

V. DISCUSSION

We have demonstrated the discrepancies between perturbative and nonperturbative methods for calculating exchange coupling parameters in various magnetic materials. For SrMnO_3 with the type-G antiferromagnetic state, the nonperturbative method reproduced the correct sign of J_{ij} under isotropic volume expansion, whereas the MFT-based method

did not. This failure was attributed to the inability of MFT-based methods to account for changes in orbital occupations and the resulting charge density differences caused by finite rotations of magnetic moments. The MFT also failed to reproduce the experimentally observed increase in the Curie temperature when substituting Fe with Co in $\text{Nd}_2\text{Fe}_{14}\text{B}$. The nonperturbative method accounts for the temperature dependence of exchange coupling parameters due to magnetic disordering, offering better agreement with experimental results. For elemental $3d$ transition metals with bcc and fcc structures, the nonperturbative method shows large discrepancies in J_{ij} at first-nearest neighbors compared to the MFT-based method. We discussed these discrepancies in terms of the angular dependence of J_{ij} and attributed them to the second-order contribution of changes in electron and magnetization densities ($\mathcal{O}(\delta n^2, \delta m^2)$) on energy variation. From these results and discussions, we again stress the importance of nonperturbative calculation of J_{ij} .

Since MFT-based methods are perturbative, they are highly compatible with Green's function methods and have a well-structured theoretical framework. This compatibility has made them a leading first-principles approach for evaluating magnetic model parameters up to the present day. However, it is important to remember that perturbative methods require careful consideration of the limits within which perturbation theory is valid. The changes in band occupancies in SrMnO_3 clearly demonstrate the limitations of the MFT-based methods. In contrast, our nonperturbative scheme offers an effective magnetic model that accounts for multiple factors, including those mentioned earlier. We plan to further develop this method and release it to the community in a user-friendly format. This advancement is expected to make the analysis and design of magnetic materials more reliable and accessible.

ACKNOWLEDGMENTS

This work was partly supported by JSPS KAKENHI Grant Number JP24K01144 and MEXT-DXMag Grant Number JPMXP1122715503. The calculations were partly carried out by using facilities of the Supercomputer Center at the Institute for Solid State Physics, the University of Tokyo, and TSUB-AME3.0 and TSUBAME4.0 supercomputers at Institute of Science Tokyo.

CONFLICT OF INTEREST

The authors declare no conflicts of interest.

-
- [1] Dey, P. & Roy, J. N. *Spintronics: Fundamentals and Applications* (Springer, Singapore, 2021). URL <https://link.springer.com/10.1007/978-981-16-0069-2>.
 [2] Eriksson, O., Bergman, A., Bergqvist, L. & Hellsvik, J. *Atomistic Spin Dynamics: Foundations and Applications* (Oxford

- University Press, 2016). URL <https://books.google.co.jp/books?id=89pJAQACAAJ>.
 [3] Mankovsky, S. & Ebert, H. First-principles calculation of the parameters used by atomistic magnetic simulations. *Electronic Structure* **4**, 034004 (2022). URL <https://dx.doi.org/10.1039/d1nr01000a>.

- 1088/2516-1075/ac89c3. Publisher: IOP Publishing.
- [4] Szilva, A. *et al.* Quantitative theory of magnetic interactions in solids. *Reviews of Modern Physics* **95**, 035004 (2023). URL <https://link.aps.org/doi/10.1103/RevModPhys.95.035004>. Publisher: American Physical Society.
- [5] Oguchi, T., Terakura, K. & Hamada, N. Magnetism of iron above the Curie temperature. *Journal of Physics F: Metal Physics* **13**, 145 (1983). URL <https://dx.doi.org/10.1088/0305-4608/13/1/018>.
- [6] Liechtenstein, A. I., Katsnelson, M. I., Antropov, V. P. & Gubanov, V. A. Local spin density functional approach to the theory of exchange interactions in ferromagnetic metals and alloys. *Journal of Magnetism and Magnetic Materials* **67**, 65–74 (1987). URL <https://www.sciencedirect.com/science/article/pii/0304885387907219>.
- [7] Terasawa, A., Matsumoto, M., Ozaki, T. & Gohda, Y. Efficient Algorithm Based on Liechtenstein Method for Computing Exchange Coupling Constants Using Localized Basis Set. *Journal of the Physical Society of Japan* **88**, 114706 (2019). URL <https://journals.jps.jp/doi/10.7566/JPSJ.88.114706>. Publisher: The Physical Society of Japan.
- [8] Nomoto, T., Koretsune, T. & Arita, R. Local force method for the ab initio tight-binding model: Effect of spin-dependent hopping on exchange interactions. *Physical Review B* **102**, 014444 (2020). URL <https://link.aps.org/doi/10.1103/PhysRevB.102.014444>. Publisher: American Physical Society.
- [9] He, X., Helbig, N., Verstraete, M. J. & Bousquet, E. TB2J: A python package for computing magnetic interaction parameters. *Computer Physics Communications* **264**, 107938 (2021). URL <https://www.sciencedirect.com/science/article/pii/S001046521000679>.
- [10] Solovyev, I. V. Exchange interactions and magnetic force theorem. *Physical Review B* **103**, 104428 (2021). URL <https://link.aps.org/doi/10.1103/PhysRevB.103.104428>. Publisher: American Physical Society.
- [11] Jacobsson, A. *et al.* Efficient parameterisation of non-collinear energy landscapes in itinerant magnets. *Scientific Reports* **12**, 18987 (2022). URL <https://www.nature.com/articles/s41598-022-20311-7>. Number: 1 Publisher: Nature Publishing Group.
- [12] Zhu, X., Edström, A. & Ederer, C. Magnetic exchange interactions in SrMnO₃. *Physical Review B* **101**, 064401 (2020). URL <https://link.aps.org/doi/10.1103/PhysRevB.101.064401>.
- [13] Solovyev, I. V. & Terakura, K. Effective single-particle potentials for MnO in light of interatomic magnetic interactions: Existing theories and perspectives. *Physical Review B* **58**, 15496–15507 (1998). URL <https://link.aps.org/doi/10.1103/PhysRevB.58.15496>. Publisher: American Physical Society.
- [14] Harashima, Y. *et al.* Data assimilation method for experimental and first-principles data: Finite-temperature magnetization of (Nd,Pr,La,Ce)₂(Fe,Co,Ni)₁₄B. *Physical Review Materials* **5**, 013806 (2021). URL <https://link.aps.org/doi/10.1103/PhysRevMaterials.5.013806>. Publisher: American Physical Society.
- [15] Antal, A. *et al.* First-principles calculations of spin interactions and the magnetic ground states of Cr trimers on Au(111). *Physical Review B* **77**, 174429 (2008). URL <https://link.aps.org/doi/10.1103/PhysRevB.77.174429>. Publisher: American Physical Society.
- [16] Togo, A., Shinohara, K. & Tanaka, I. Spglib: a software library for crystal symmetry search (2024). URL <http://arxiv.org/abs/1808.01590>. ArXiv:1808.01590 [cond-mat].
- [17] Heine, M., Hellman, O. & Broido, D. Temperature-dependent renormalization of magnetic interactions by thermal, magnetic, and lattice disorder from first principles. *Physical Review B* **103**, 184409 (2021). URL <https://link.aps.org/doi/10.1103/PhysRevB.103.184409>. Publisher: American Physical Society.
- [18] Sandratskii, L. M. Noncollinear magnetism in itinerant-electron systems: Theory and applications. *Advances in Physics* **47**, 91–160 (1998). URL <https://doi.org/10.1080/000187398243573>. Publisher: Taylor & Francis eprint: <https://doi.org/10.1080/000187398243573>.
- [19] Drautz, R. & Fähnle, M. Spin-cluster expansion: Parametrization of the general adiabatic magnetic energy surface with ab initio accuracy. *Physical Review B* **69**, 104404 (2004). URL <https://link.aps.org/doi/10.1103/PhysRevB.69.104404>. Publisher: American Physical Society.
- [20] Blöchl, P. E. Projector augmented-wave method. *Phys. Rev. B* **50**, 17953–17979 (1994).
- [21] Kresse, G. & Furthmüller, J. Efficient iterative schemes for ab initio total-energy calculations using a plane-wave basis set. *Phys. Rev. B* **54**, 11169–11186 (1996).
- [22] Kresse, G. & Joubert, D. From ultrasoft pseudopotentials to the projector augmented-wave method. *Phys. Rev. B* **59**, 1758–1775 (1999).
- [23] Perdew, J. P. *et al.* Restoring the Density-Gradient Expansion for Exchange in Solids and Surfaces. *Physical Review Letters* **100**, 136406 (2008). URL <https://link.aps.org/doi/10.1103/PhysRevLett.100.136406>. Publisher: American Physical Society.
- [24] Perdew, J. P., Burke, K. & Ernzerhof, M. Generalized Gradient Approximation Made Simple. *Phys. Rev. Lett.* **77**, 3865–3868 (1996).
- [25] Dudarev, S. L., Botton, G. A., Savrasov, S. Y., Humphreys, C. J. & Sutton, A. P. Electron-energy-loss spectra and the structural stability of nickel oxide: An LSDA+U study. *Physical Review B* **57**, 1505–1509 (1998). URL <https://link.aps.org/doi/10.1103/PhysRevB.57.1505>. Publisher: American Physical Society.
- [26] Roux, D. L., Vincent, H., L'Héritier, P. & Fruchart, R. CRYSTALLOGRAPHIC AND MAGNETIC STUDIES OF Nd₂Co₁₄B AND Y₂Co₁₄B. *Journal de Physique Colloques* **46**, C6 (1985). URL <https://hal.science/jpa-00224895>.
- [27] Herbst, J. F., Croat, J. J. & Yelon, W. B. Structural and magnetic properties of Nd₂Fe₁₄B (invited). *Journal of Applied Physics* **57**, 4086–4090 (1985). URL <https://doi.org/10.1063/1.334680>.
- [28] Matsubara, F. & Inawashiro, S. Mixture of Two Anisotropic Antiferromagnets with Different Easy Axes. *Journal of the Physical Society of Japan* **42**, 1529–1537 (1977). URL <https://journals.jps.jp/doi/10.1143/JPSJ.42.1529>. Publisher: The Physical Society of Japan.
- [29] Pizzi, G. *et al.* Wannier90 as a community code: new features and applications. *Journal of Physics: Condensed Matter* **32**, 165902 (2020). URL <https://dx.doi.org/10.1088/1361-648X/ab51ff>. Publisher: IOP Publishing.
- [30] Akai, H. Fast Korringa-Kohn-Rostoker coherent potential approximation and its application to FCC Ni-Fe systems. *Journal of Physics: Condensed Matter* **1**, 8045 (1989). URL <https://dx.doi.org/10.1088/0953-8984/1/43/006>.

- [31] Rezaei, N., Alaei, M. & Akbarzadeh, H. ESpinS: A program for classical Monte-Carlo simulations of spin systems. *Computational Materials Science* **202**, 110947 (2022). URL <https://www.sciencedirect.com/science/article/pii/S0927025621006431>.
- [32] Edström, A. & Ederer, C. First-principles-based strain and temperature-dependent ferroic phase diagram of SrMnO₃. *Physical Review Materials* **2**, 104409 (2018). URL <https://link.aps.org/doi/10.1103/PhysRevMaterials.2.104409>. Publisher: American Physical Society.
- [33] Maurel, L. *et al.* Nature of antiferromagnetic order in epitaxially strained multiferroic SrMnO₃ thin films. *Physical Review B* **92**, 024419 (2015). URL <https://link.aps.org/doi/10.1103/PhysRevB.92.024419>. Publisher: American Physical Society.
- [34] Wang, V., Xu, N., Liu, J.-C., Tang, G. & Geng, W.-T. VASPKIT: A user-friendly interface facilitating high-throughput computing and analysis using VASP code. *Computer Physics Communications* **267**, 108033 (2021). URL <https://www.sciencedirect.com/science/article/pii/S0010465521001454>.
- [35] Momma, K. & Izumi, F. VESTA 3 for three-dimensional visualization of crystal, volumetric and morphology data. *Journal of Applied Crystallography* **44**, 1272–1276 (2011). URL <https://journals.iucr.org/j/issues/2011/06/00/db5098/>. Publisher: International Union of Crystallography.
- [36] Miyake, T., Harashima, Y., Fukazawa, T. & Akai, H. Understanding and optimization of hard magnetic compounds from first principles. *Science and Technology of Advanced Materials* **22**, 543–556 (2021). URL <https://doi.org/10.1080/14686996.2021.1935314>. Publisher: Taylor & Francis. eprint: <https://doi.org/10.1080/14686996.2021.1935314>.
- [37] Gohda, Y. First-principles determination of intergranular atomic arrangements and magnetic properties in rare-earth permanent magnets. *Science and Technology of Advanced Materials* **22**, 113–123 (2021). URL <https://doi.org/10.1080/14686996.2021.1877092>. Publisher: Taylor & Francis. eprint: <https://doi.org/10.1080/14686996.2021.1877092>.
- [38] Seo, I., Tanaka, S., Endo, M. & Gohda, Y. Prediction of NdFe₁₆-based permanent-magnet compounds with high magnetization. *Applied Physics Express* **17**, 075502 (2024). URL <https://dx.doi.org/10.35848/1882-0786/ad5fd9>. Publisher: IOP Publishing.
- [39] Sagawa, M., Fujimura, S., Togawa, N., Yamamoto, H. & Matsuura, Y. New material for permanent magnets on a base of Nd and Fe (invited). *Journal of Applied Physics* **55**, 2083–2087 (1984). URL <https://doi.org/10.1063/1.333572>.
- [40] Fuerst, C. D. & Herbst, J. F. Hard magnetic properties of Nd-Co-B materials. *Journal of Applied Physics* **64**, 1332–1337 (1988). URL <https://doi.org/10.1063/1.341855>.
- [41] Tsuna, S. & Gohda, Y. First-principles phonon calculations of neodymium-magnet compounds. *Journal of Applied Physics* **133**, 115103 (2023). URL <https://doi.org/10.1063/5.0142945>.
- [42] Tanaka, T. & Gohda, Y. Prediction of the Curie temperature considering the dependence of the phonon free energy on magnetic states. *npj Computational Materials* **6**, 1–7 (2020). URL <https://www.nature.com/articles/s41524-020-00458-5>. Publisher: Nature Publishing Group.
- [43] Mankovsky, S., Polesya, S. & Ebert, H. Extension of the standard Heisenberg Hamiltonian to multispin exchange interactions. *Physical Review B* **101**, 174401 (2020). URL <https://link.aps.org/doi/10.1103/PhysRevB.101.174401>. Publisher: American Physical Society.
- [44] Antropov, V. P. The exchange coupling and spin waves in metallic magnets: removal of the long-wave approximation. *Journal of Magnetism and Magnetic Materials* **262**, L192–L197 (2003). URL <https://www.sciencedirect.com/science/article/pii/S0304885303002063>.
- [45] Haynes, W. (ed.) *CRC Handbook of Chemistry and Physics* (CRC Press, 2014), 95th edn.
- [46] Fawcett, E. Spin-density-wave antiferromagnetism in chromium. *Reviews of Modern Physics* **60**, 209–283 (1988). URL <https://link.aps.org/doi/10.1103/RevModPhys.60.209>. Publisher: American Physical Society.
- [47] Tanaka, T. & Gohda, Y. First-Principles Study of Magnetism-Dependent Phonons Governed by Exchange Ligand Field. *Journal of the Physical Society of Japan* **89**, 093705 (2020). URL <https://journals.jps.jp/doi/10.7566/JPSJ.89.093705>. Publisher: The Physical Society of Japan.